Directed Energy Deposition Processing-Performance Relationship of AF9628

M. Yang[1], M. M. Parvez[1], T, Sparks[3], S. Babalola[2], J. W. Newkirk[2], K. Chandrashekhara[1], L. N. Bartlett[2], and F. Liou[1]

[1]Department of Mechanical and Aerospace Engineering
[2]Department of Materials Science and Engineering
Missouri University of Science and Technology, Rolla, MO 65409
[3]Product Innovation and Engineering, LLC, St. James, MO 65559

Abstract

AF9628 low alloy steel is a novel steel known for its low cost, high hardness, and outstanding tensile performance. However, the processing methods of AF9628 have been less studied in the additive manufacturing field. As the balance of hardness and tensile results is closely related to the cooling process during manufacturing process window and its relationship to resultant tensile properties was explored. By using the DED method, specimens of this steel were successfully fabricated, and tensile test results were obtained. The AF9628 steel can be manufactured for tailored properties with the DED process by controlling the cooling method. This work was funded by ARL - GVSC under cooperative agreement W911NF-20-2-0251.

Keywords: Directed Energy Deposition (DED), AF9628 Low Alloy Steel, Laser Power, Scan speed, Cooling Rate, Micro-tensile Test (YS, UTS, Elongation).

Introduction

AF9628 is a novel alloy invented by the U.S. Air Force. Its high tensile strength and low cost enables it to be an outstanding material. The AF9628 has been widely studied with selective laser melting (SLM) process. A mean YS (yield strength) of over 1500MPa, a mean UTS (Ultimate tensile strength) of over 1700Mpa, and a mean elongation of over 10% were tensile tested along and perpendicular to the build direction [1]. However, the AF9628 low alloy steel has been rarely studied in the DED (direct energy deposition) process. It is likely that the tensile strength (YS, UTS, elongation) of the AF9628 alloy steel can be further improved. Once it is improved, the AF9628 low alloy steel can also become an ideal material for 3D rapid repair. This paper includes the study of the tensile results from the AF9628 DED process.

Experimental Setup

The AF9628 low alloy is developed by Dr. Rachel Abrahams. This type of novel alloy interests the industry for its ultra high-strength and low cost. As costly element such as Ni is limited, the cost of AF9628 is lower than the conventional alloy steel. It is also highly weldable since it does not contain any high melting point elements such as W or Ti. All these properties make the AF928 steel an attractive material for additive manufacturing process, which makes it doable to produce parts of more complex geometry. [1]

Material:

The AF9628 low alloy powder used in this study was the commercial AM powder produced by Powder Alloy Corporation. The AF9628 particle size was analyzed by the AFA mode on the ASPEX Machine. The powder images (shown in Figure 1a.) were taken ranging from x120 through x 200. As shown in these images, the AF9628 powders purchased for this study were not perfectly spherical. [12,14] Some of the particles were in an elliptical shape.
AF9628 Particle Size Distribution:

The particle distribution is shown in Figure 1b. There were 5028 particles analyzed in size. According to Davg, about 39% of the particles were very fine(<10µm) 45% of the particles were fine(10-20µm)13 % of the particles were 20-60µm, and ~3% of the particles were >60µm. The particle size majorly ranges between 5-20 microns. The max population was found between 5-10 microns.

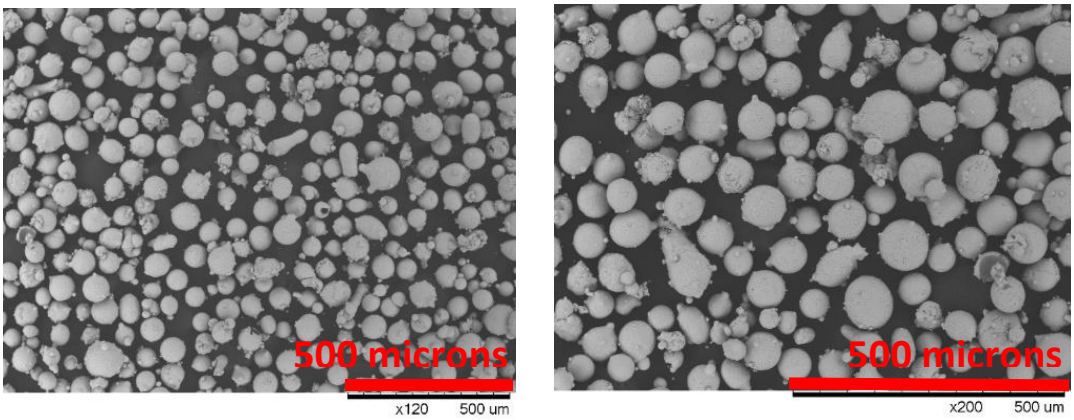

Figure 1a. AF9628C powder SEM image at higher and lower magnifications

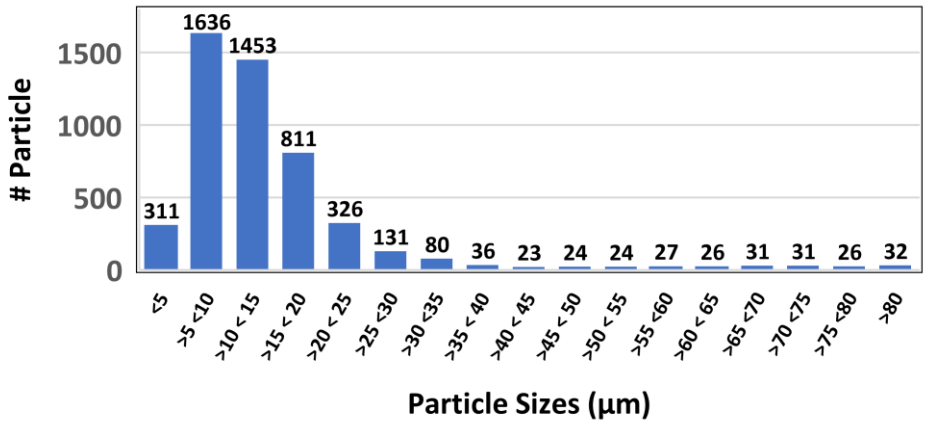

Figure 1b. AF9628C Particle Distribution

The AF9628 low alloy powder used in this study was the commercial AM powder produced by Powder Alloy Corporation. The chemical composition from literature review is listed below for reference (Table 1).

Table 1 Chemical composition by weight percent of AF9628 [2]

Element	O	C	S	H	Mn	Si	P	Cr
Weight (%)	0.028	0.28	<0.005	0.0002	0.7	0.9	<0.01	2.8
Element	Ni	Mo	Cu	V	Al	Ti	P+Sn+As+Sb	Fe
Weight (%)	1.1	1	<0.1	0.12	0.009	0.004	<0.035	Balance

The Powder density tester used in this study was "Ultrapyc 1200e" the results are shown in Figure 1c.

		Run							
SI#	mass (gm)	#1 V(cc)	#2 V(cc)	#3 V(cc)	#1 density (g/cc)	#2 density (g/cc)	#3 density (g/cc)	Average Density (g/cc)	STD
1	21.257	2.727	2.729	2.728	7.793	7.790	7.792	7.791	0.0005
2	12.663	1.627	1.627	1.628	7.781	7.781	7.774	7.779	0.0006
3	17.668	2.272	2.275	2.274	7.777	7.766	7.769	7.770	0.0013

Figure 1c. Ultrapyc 1200e. Experimental settings: Nitrogen gas, Pressure: 10 PSI, Pulse: 3, Run: 3 Randomization applied: 21.257 gm, 12.663 gm, 17.668 gm. $Gas\ pore\ density$: 0.475 ±0.119 (%). Theatrically powder density: 7.818 g/cc

Experiment procedure and design:

The AM system used in this study equipped a maximum 1000w fiber laser with a 2mm diameter laser beam, an electrostatic wheel feeder with the feed rate set at 1.8 g/min. All the equipment was controlled by the LinuxCNC software.

This study was focused on single track geometry of dimensions 45 mm x 2.5 mm x 15 mm. The layer thickness was 0.2 mm (75 layers). The simply left and right moving tool path shown in Figure 2 was used in this study. To control the delay time and keep the gantry moving at a constant jogging speed, the gantry was programmed to move for a pre-calculated extra distance of 17 mm, so that the gantry jogs left and right at the scan speed of 200 mm/min to keep the 10 seconds delay time. Once the gantry jogs to the very end of each direction the gantry lowers for 0.2 mm (set up thickness) then goes back to either the left or right edge of the geometry end. Once the gantry arrives at the edge of the geometry, the deposition of the next layer starts.

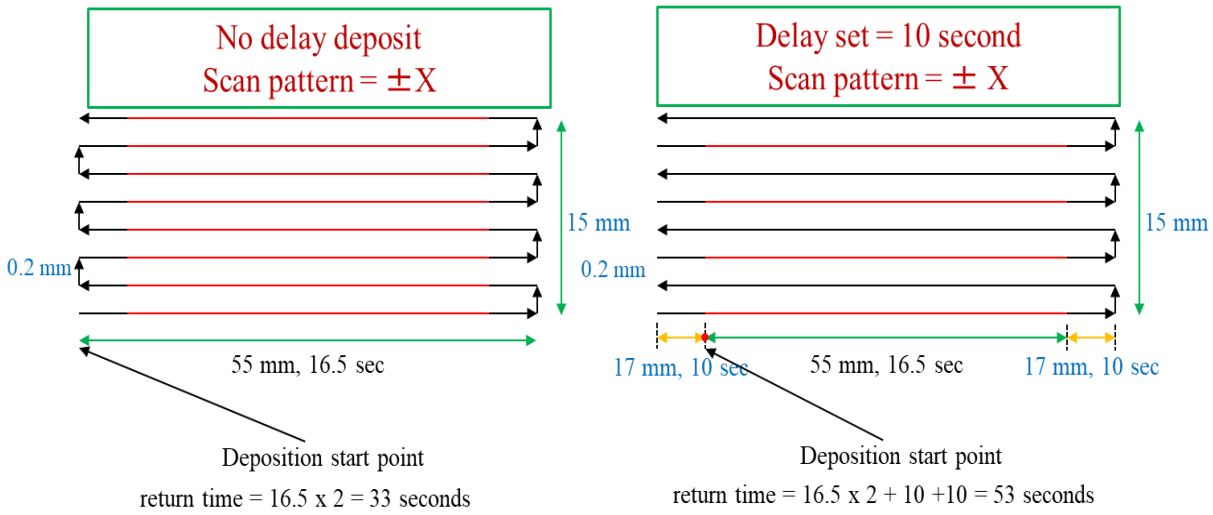

Figure 2. Single-track tool path. Delay calculation: Scan speed = 200 mm/min delay time = (17x2) / (200/60) = 10 seconds

The substrate used for AF9628 single track deposition was SS304 of a dimension of 5mm x 10mm x 55mm. A 350w laser power was used for preheating and the experiment parameters are shown in Table 2.

Table 2. Single track DED deposition process parameters of samples #1 through #11

Sample #	Layer width (mm)	Layer Thickness (mm)	Scan Speed (mm/min)	Laser power (W)	Delay (s)
1			200	350	10
2			200	400	10
3			150	300	no delay
4			200	300	no delay
5			250	300	no delay
6	2.5	0.2	150	350	no delay
7			200	350	no delay
8			250	350	no delay
9			150	400	no delay
10			200	400	no delay
11			250	400	no delay

To avoid the sample being oxidized, argon supply was kept on for at least 15 mins to make sure the sample cools down below the oxidization temperature before collecting the sample.

Characterization:

After the micro tensile samples were tested, the broken pieces were collected and mounted with epoxy for micro-structure observation. The polisher used in this study was MEPREP3 PH-3. The samples were polished to 0.05. After polishing the samples, the SEM images were taken under with EBSD to investigate the phases of sample 1 and sample 2.

Mechanical Testing:

Once the sample was deposited, the single-track deposition as well as the substrate were sliced vertically with EDM into 1 mm thickness pieces, the MT2 samples were extracted along the build direction side by side shown in figure 3(a). Rough finish (polish) with 800 grit sandpaper to remove the surface oxide, take the measurement with the micrometer for the width and thickness of the middle flask of the MT2 samples, and record the dimensions of the micro-tensile sample. The theorical dimensions of the MT2 samples are shown in figure 3(a). Repeating the process for all pieces, once the dimension table of the MT2 samples was made, then the samples were prepared.

Figure 3(a). Locations where the micro-tensile samples were extracted from a 1mm thick slice
Figure 3(b). Dimensions of the micro-tensile samples

The tensile tester used in this study was INSTRON accompanied with an ex-tensile meter and Bluehills3 control program. It has a 50 kN maximum stress. The tensile test parameters were 0.015mm/mm/min test speed and 1.5mm/min rate 2.

After the micro-tensile samples were tested, the debris were collected (shown in Figure 4a) and prepared for Vickers-hardness test. The hardness tester used in this study was “Struers Duramin5”. On each piece of debris, three locations (shown in Figure 4b) were put along x-axis, perpendicular to the build direction on the wide end of each piece, three indents were put at each location to calculate the mean local hardness value. In total, twelve locations (36 indents) of each sample were tested for the global hardness value. All indents were tested by the parameters set at 9.81N 10 seconds and 40x magnification shown in table 6.

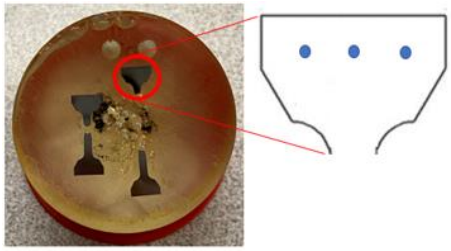

(a) (b)

Figure 4a. Four pieces of prepared micro-tensile debris of sample 2 in one epoxy mount for hardness test
Figure 4b. Three Vickers-hardness tested locations on one piece of micro-tensile debris labeled in blue color.

Results and Discussion

Microstructure:

The porosity morphology shown in figure 5a sample 1 could indicate lack of fusion defects as the irregular defects were observed. In figure 5a sample 2 the porosity is evenly distributed, which could indicate outgassing in this higher energy density specimen.

As what is shown in figure 5b, the phase mappings of sample 1 and 2 are showing different phase morphologies. Comparing with sample 2 the phases size of sample 1 are more uniform.

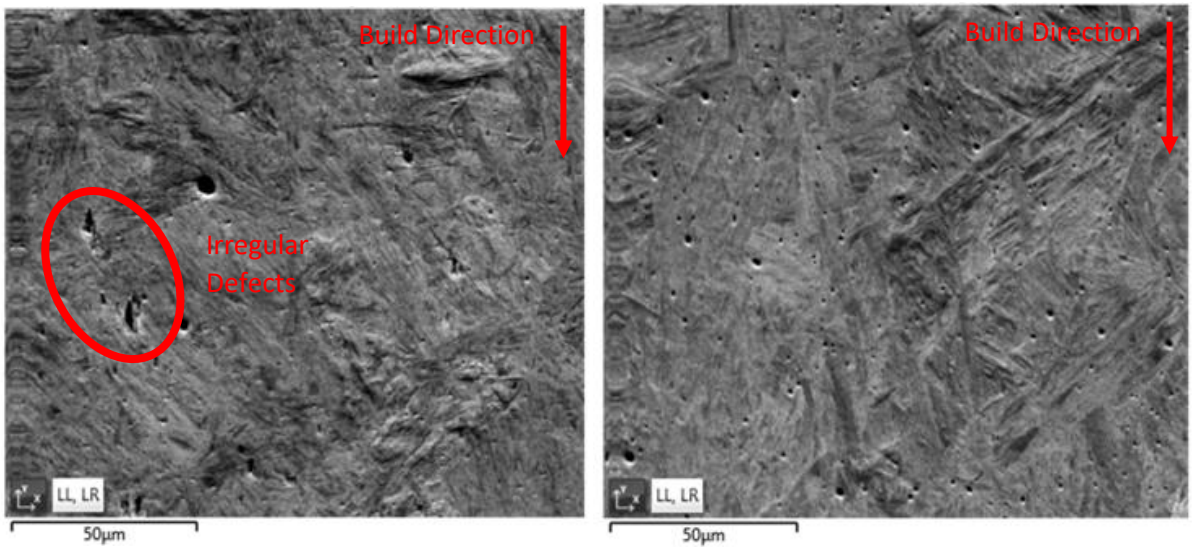

Sample 1 Sample 2

Figure 5a. Sample 1 & 2 EBSD fore scattered detector (FSD) images for porosity comparison

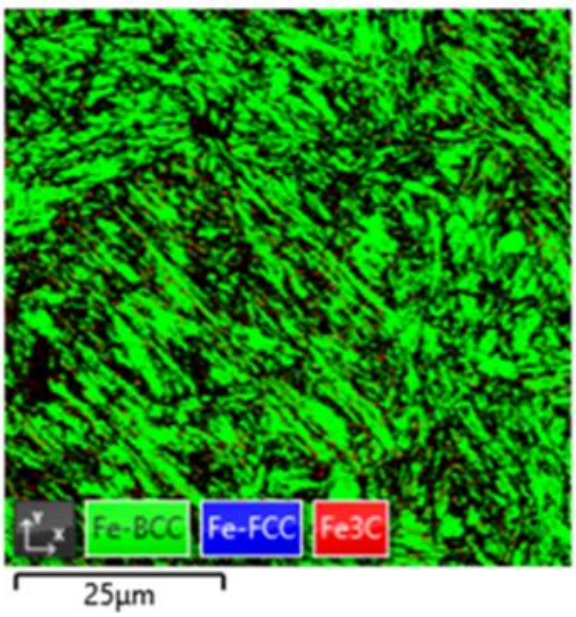

Sample 1 phase color

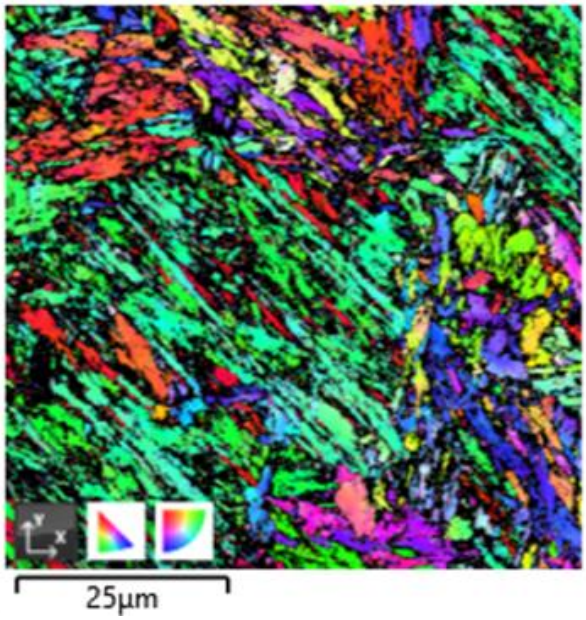

Sample 1 IPF color

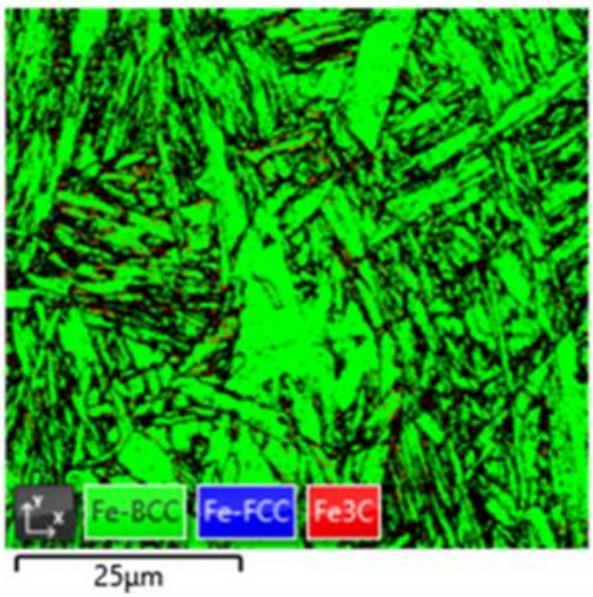

Sample 2 phase color

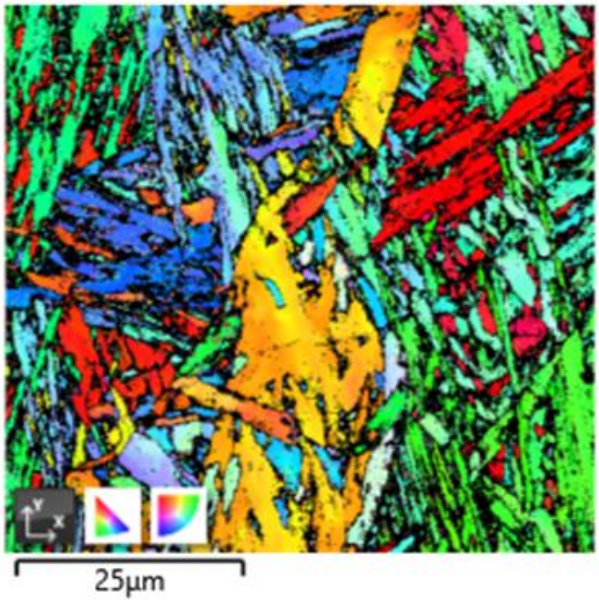

Sample 2 IPF color

Figure 5b. Sample 1 & 2 phase mappings for phase size comparison

In this study, ferrite and cementite phases were specifically focused to find Bainite. As what is shown in Table 3, assuming the total carbon content of both samples is similar, the lower rate of a discrete carbide phase in sample 2 could indicate a higher prevalence of bainite than in sample 1. Potentially more austenite phases are transformed into Bainite during the transforming stage of the cooling process in sample #2.

Table 3. DED sample 1 and 2 mapping analysis

	Sample 1		Sample 2	
Phase Name	Phase Fraction (%)	Phase Count	Phase Fraction (%)	Phase Count
Fe-BCC	49.67	97025	59.18	99581
Fe-FCC	0.25	497	0.29	485
Fe3C	4.53	8846	2.95	4959
Zero Solutions	45.55	88971	37.59	63245
*Grain Diameter Median [µm]	1.5		0.9	

* Mean grain diameter analyzed with phases over 10 pixels

Sample 2's highest frequency bin (shown in Histogram 1) is the sub-micron category, indicating that the median grain size is much smaller than sample 1. The smaller median grain size in sample #2 supports the tensile result of sample #2 tested a higher UTS than sample #1 [13].

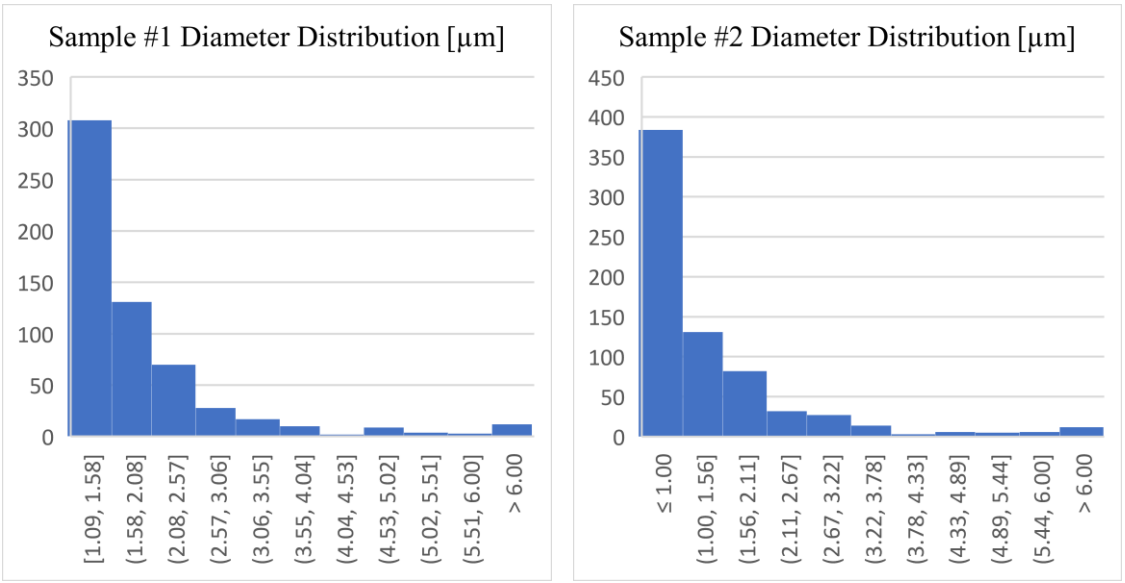

(a) (b)

Histogram 1. Sample #1 & #2 Grain Diameter Distributions [µm]

Tensile Properties

Eleven samples were tested under the same tensile test parameters in this study. Both sample 1 and sample 2 were deposited at 200 mm/min and 10 seconds delay between each layer, but sample one was processed with 350 W laser power, and sample two was processed with 400 W laser power. The tensile results of sample 1 and sample 2 were shown in Figures 6a, 6b and compared with other tensile results in table 5.

Sample 1 and sample 2 were both tested for over 900 MPa yield strength and a relatively high elongation of over 20% [14,15] as shown in Figure 6a and 6b. Sample one was tested slightly higher than sample 1 based on the calculated mean YS values and mean elongation percentages. However, a mean ultimate-tensile strength of over 1800 MPa was tested in sample two, which was about 400 MPa (28%) higher than sample 2.

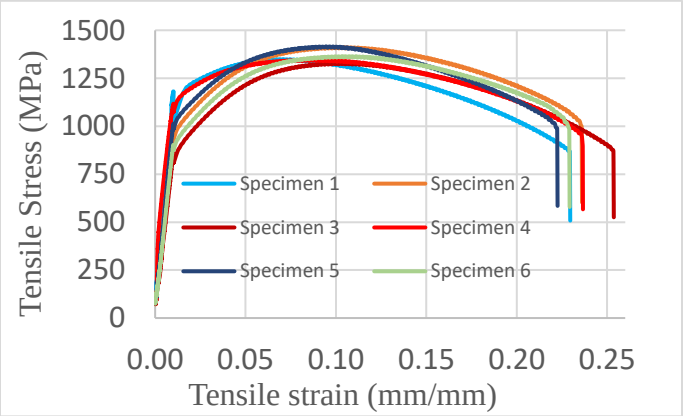

Scan speed	200 mm/min
Layer width	2.50 mm
Layer thickness	0.20 mm
Laser Power	350 W

	YS (MPa)	UTS (MPa)	Elongation (%)
Mean	975	1365	22.8
Median	972	1349	22.9
S.D.	106	35	1.90

Figure 6a. stress-strain curve process parameters and tensile results of sample 1, 200 mm/min scan speed, 10s delay between each layer 350 W laser power.

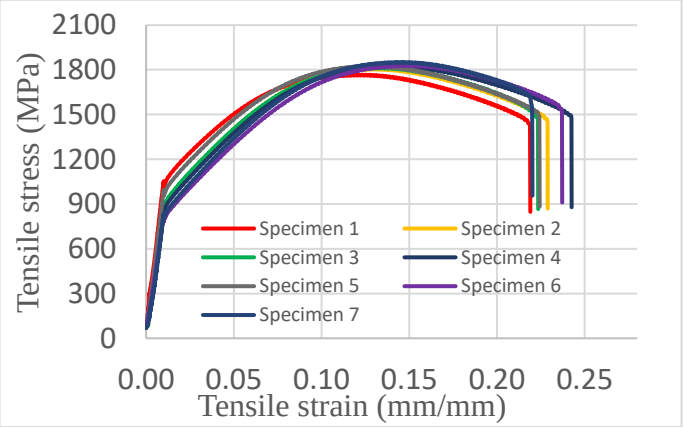

Scan speed	200 mm/min
Layer width	2.50 mm
Layer thickness	0.20 mm
Laser Power	400 W

	YS (MPa)	UTS (MPa)	Elongation (%)
Mean	958	1806	21.8
Median	937	1819	22.3
S.D.	94	40	2.80

Figure 6b. stress-strain curve process parameters and tensile results of sample 2, 200 mm/min scan speed, 10s delay between each layer 400 W laser power.

The tensile results of samples deposited with no delay between each layer are shown in Figure 6c (i) through 6c (iii). None of the nine consciously deposited samples was tensile tested for an over 1600 MPa UTS or an over 15% elongation. Sample #5 and sample #11 tested a mean UTS value close to 1500 MPa. Relatively uniform elongation percentages were tested on the no delay samples. The elongation range was between 6% to 8%. The yield strength distribution was tested around 1000 MPa, and the highest mean yield strength was tested 1100 MPa at sample #5.

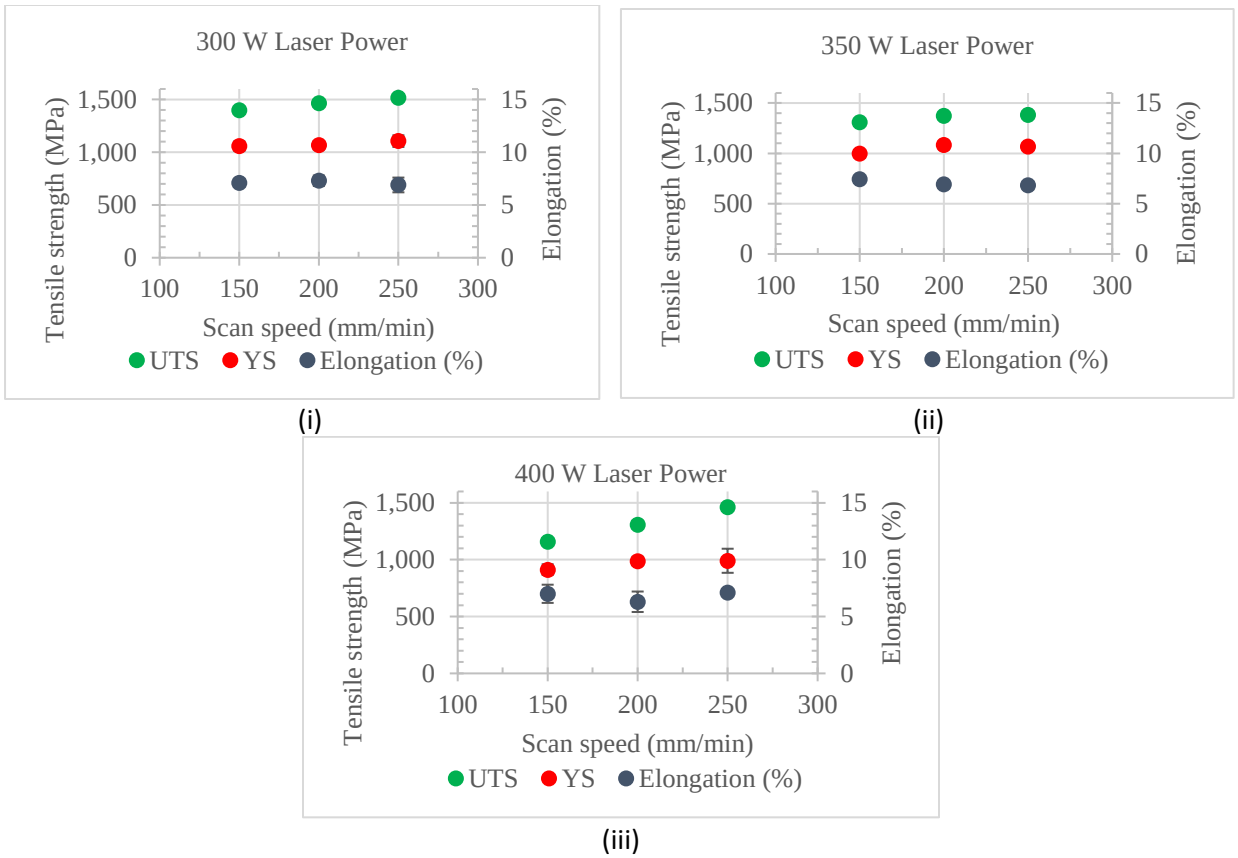

Figure 6c. Tensile results of (i) 300W, (ii) 350W, (iii) 400W laser power no delay samples at different Scan Speeds

Sample one and sample two tested relatively the same yield strength as the cast AF9628 steel shown in Figure 6d, and the UTS of sample 1 was tested relatively the same as the cast AF9628. However, the UTS of sample 2 was 400 MPa higher than the UTS of the cast AF9628, and both sample 1 and sample 2 were tested about 7% higher than the cast AF9628 in mean elongation.

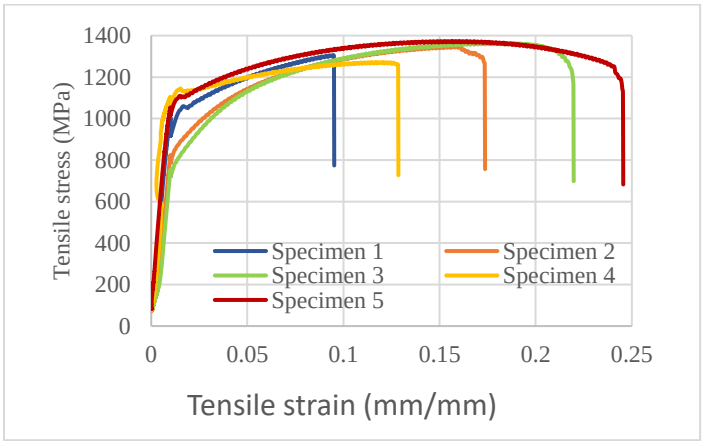

	YS (MPa)	UTS (MPa)	Elongation
Mean	978	1339	15.4
Median	983	1356	15.0
S.D.	150	41	7.10

Figure 6d. Cast AF9628 stress-strain curve and tensile results

Sample one deposited in this study was tested about 100 MPA lower in YS compared with the SLM processed AF9628 tested at both vertical direction and horizontal directions. However, the UTS of the SLM processed AF9628 was about 100 MPa lower than sample 1 and 500 MPa lower than sample 2., and the mean elongation of sample one and sample two were both 50% high than the SLM processed AF9628 compared with [5] shown in Figure 6e.

The YS in [1] shown in table 4. was about 500 MPa higher than either sample 1 or sample 2, and the UTS of [1] was 300 MPa higher than sample 1 but 100 MPa lower than sample 2 in all tested directions. However, the elongation of sample 1 and sample 2 were both about twice of the elongation percentage of the [1] results in all directions.

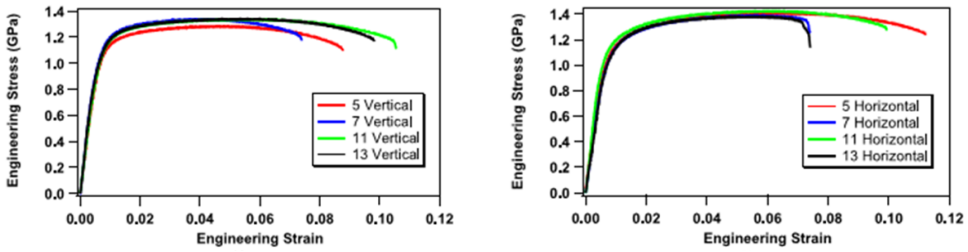

Figure 6e. AF9628 SLM process stress-strain curve from [5]

Table 4. AF9628 SLM process tensile results from [1] where TD-SD refers to XY plane (horizontal direction) SD-BD refers to YZ plane (vertical direction) BD-TD refers to XZ plane (vertical direction)

Sample orientation	YS (MPa)	UTS (MPa)	Elongation (%)
TD - SD	1530 ± 8	1700 ± 3	11.5 ± 0.4
SD - BD	1523 ± 7	1700 ± 5	10.8 ± 0.5
BD - TD	1526 ± 5	1705 ± 3	10.5 ± 0.7

Table 5. AF9628 tensile comparison of different processes in energy density, ultra-tensile strength, yield strength, and elongation

AF9628 Processes	ED (J/mm^3)	UTS (MPa)	YS (MPa)	Elongation (%)
DED (No Delay)	240	1309	988	6.3
DED (10 S Delay)	240	1806	958	21.8
Cast	n/a	1339	978	15.4
SLM [5]	Not given	1700	1530	11.5
SLM [1]	60.1	1420	1100	7.71

The ductile fracture surfaces shown in Figures 7a (i) and 7a (ii), and Figures 7b (i) and 7b (ii) were observed at both sample 1 and sample 2. No sign of brittle surface was observed at sample 1 or sample 2. Sample 1 and sample 2 have a similar surface texture at x500 magnification. The overview at low magnification of sample 1 fracture surface was observed to be finer and slightly more uniform than the overview of sample 2 fracture surface. However, a larger pore defect was seen at the corner of sample 1 fracture surface. Sample 1 had a higher defect density than sample 2, which resulted in sample 2 being tested with a much higher UTS than sample 1 in the tensile test.

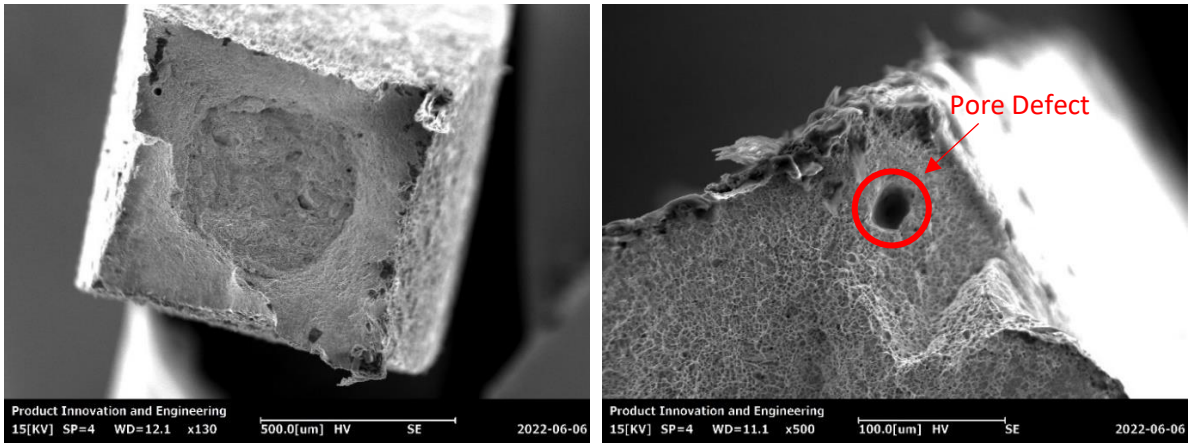

(i) (ii)

Figure 7a (i). Sample 1 fracture surface SEM image overview
Figure 7a (ii). Sample 1 fracture surface SEM image at the conner of the fracture surface

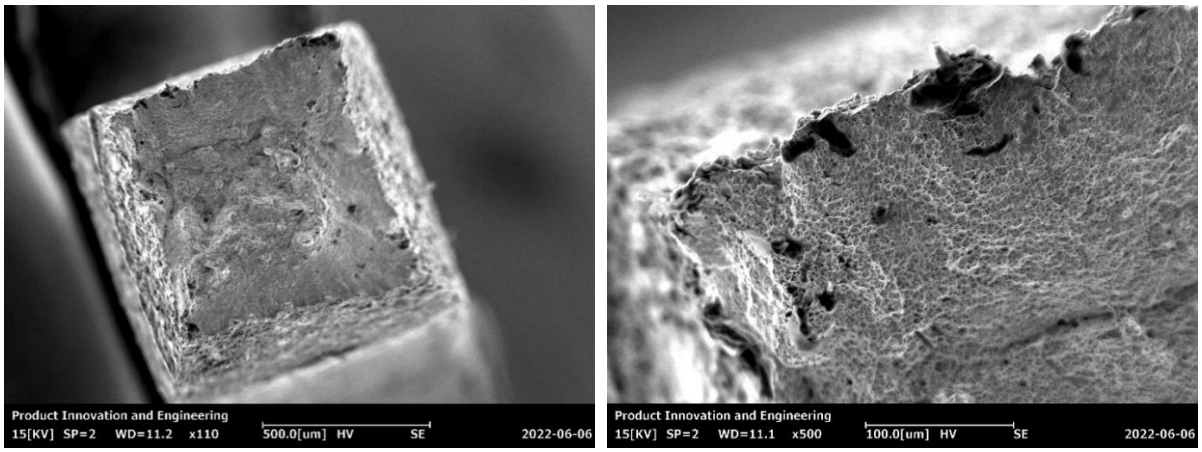

(i) (ii)

Figure 7b (i). Sample 2 fracture surface SEM Image at x110 magnification overview
Figure 7b (ii). Sample 2 fracture surface SEM Image at x500 magnification at the conner of the fracture surface

Hardness Properties

	Sample 1	Sample 2	Sample 5	Sample 8
Laser Power (W)	350	400	300	350
Scan Speed (mm/min)	200	200	250	250
Delay B/W Layers (s)	10		No Delay	
Press Force (N)	9.81			
Press Time (s)	10			
Magnification	40x			
Mean Hardness (HV)	437	429	480	481
Global S.D.	8	8	10	9

Table 6. Samples 1 2 5 8 mean Vickers-hardness values referring to process parameters and test parameters

All the 11 samples were tested at room temperature for Vickers-hardness, and all samples were tested for relatively high Vickers-hardness values. [6,7,8,9,10,11]. The results of samples 1 2 5 and 8 were selected for comparison, their hardness results are shown in table 6. Sample 1 and sample 2 were deposited with 10 seconds delay between each layer, and sample 5 and sample 8 were without delay between each layer. Based on the global mean hardness value, sample 1 was closer to sample 2 in hardness, both were around 430 HV. Sample 1 was tested 8 HV higher than sample 2. Both sample 5 and sample 8 tested about 480 HV, and both were 35 HV higher than sample 1 and sample 2.

The parameter differences of laser power and scan speed played a minor factor in the variance of sample Vickers-hardness. The factor leading to the major difference in Vickers-hardness results can be the different cooling rates. When the sample was deposited with 10 seconds delay, the sample cooled down more compared to a layer-by-layer process. The temperature was further decreased, the grains can be formed more completely when each layer was scanned comparing with the samples deposited without delay between each layer. The cooling rate of the samples deposited without delay was more compared to the cast process, as the cooling time between each layer was shorter, the whole part cooled down as an entire body, hence resulted the sample in a higher Vickers-hardness.

Conclusions

The AF9628C low steel alloy tensile property was related to its hardness property. One relatively increases as the other relatively decreases. The cooling rate was a significant factor for AF9628C low steel alloy to weigh the properties. A process of 10 s delay between each layer resulted in higher values in UTS and elongation, as well as lower values in YS and hardness. A process of no delay between each layer resulted in higher values in YS and hardness, along with lower values in UTS and elongation.

- Tensile Properties

  Both sample 1 and sample 2 with 10 seconds delay were tested over 20% elongation, whereas the samples processed with no delay were all tested less than 10% elongation. An over 1800 MPa mean UTS was tested at Sample 2. However, the YS of sample 1 and sample 2 were both tested about 100 to 150 MPa lower than other samples processed with no delay between each layer. As the longer delay between each layer, the more heat will be emitted and conducted, the alloy grain can be more evenly formed. As the alloy grains were formed evenly, the stress was more uniformly distributed on the sample body and less likely to accumulate over the break threshold at one point as the elongated distance increased, hence higher elongation percentage and UTS were tested at sample 2.

- Hardness Properties

  Sample 1 and sample 2 were tested relatively lower Vickers-hardness values than the samples processed with no delay between each layer. The difference in Vickers-hardness results can be sourced to the different cooling rate. The over low melt pool cooling rate during solid-state phase transformation transformed mostly Austenite into Pearlite and the over high cooling rate during solid state phase transformation transformed Austenite mostly into Martensite. Both the Pearlite and Martensite can result the sample in higher hardness results [16,17]. The melt pool temperature in both delay and no delay processes were relatively constant when melt pools were formed. The melt pools of the samples deposited with no delay solidified and transformed slower as the cooling time between each laser scan was shorter, less heat conducted, the temperature of the solidified part of the sample was higher, the melt pool solidified and transformed under low temperature deference between the melt pool and the early solidified part of the sample. In addition, the melt pools of the samples deposited with delay solidified and transformed faster as the cooling time between each laser scan was longer, more heat conducted, the temperature of the early solidified part of the sample was lower, the melt pool solidified and transformed under high temperature deference between the melt pool and the early solidified part of the sample.

The melt pool firstly solidified into Austenite. Bainite can only be transformed from Austenite within certain temperature region during the solid-state phase transformation. The temperature decreasing paths of each sample were nonlinear in both delay and no delay deposition processes. The cooling time in each temperature regions could be different from sample to sample and layer to layer during each heating and cooling cycle. The different dwell time at each temperature region resulted in different percentages of Austenite were transformed

into Bainite phases during each solid-state phase transformation after the melt pool solidified into Austenite [18,19]. In this study, the factor of the samples with 10 seconds delay turned to be more durable than the samples processed with no delay can be that the time delay kept the Austenite temperature changing paths a longer time within the Bainite forming region, hence higher percentages of phase were transformed into Bainite during the solid-state phase transformation in those samples with 10 s delay. Above all, the AF9628 steel can be manufactured for tailored properties with the DED process by verifying the cooling method.

Acknowledgments

This work was funded by ARL - GVSC under cooperative agreement W911NF-20-2-0251.

References

[1] P. Agrawal et al., "Microstructure–Property Correlation in a Laser Powder Bed Fusion Processed High-Strength AF-9628 Steel," Adv. Eng. Mater., vol. 23, no. 1, p. 2000845, Jan. 2021, doi: 10.1002/adem.202000845.

[2] E. M. Hager et al., "Development of high density parts in the low-alloy, high-performance steel AF9628 using laser powder bed fusion," Materials Science and Engineering: A, vol. 838, p. 142656, Mar. 2022, doi: 10.1016/j.msea.2022.142656.

[3] R. Seede et al., "Effect of heat treatments on the microstructure and mechanical properties of an ultra-high strength martensitic steel fabricated via laser powder bed fusion additive manufacturing," Additive Manufacturing, vol. 47, p. 102255, Nov. 2021, doi: 10.1016/j.addma.2021.102255.

[4] C. Tan et al., "Superior strength-ductility in laser aided additive manufactured high-strength steel by combination of intrinsic tempering and heat treatment," Virtual and Physical Prototyping, vol. 16, no. 4, pp. 460–480, Jul. 2021, doi: 10.1080/17452759.2021.1964268.

[5] R. Seede et al., "An ultra-high strength martensitic steel fabricated using selective laser melting additive manufacturing: Densification, microstructure, and mechanical properties," Acta Materialia, vol. 186, pp. 199–214, Mar. 2020, doi: 10.1016/j.actamat.2019.12.037.

[6] C. R. Hasbrouck, A. S. Hankey, R. Abrahams, and P. C. Lynch, "Sub-Surface Microstructural Evolution and Chip Formation During Turning of AF 9628 Steel," Procedia Manufacturing, vol. 48, pp. 559–569, 2020, doi: 10.1016/j.promfg.2020.05.083.

[7] P. Chaitanya, R. Goud, R. Raghavan, M. Ramakrishna, K. G. Prashanth, and S. Gollapudi, "Technical Note: Hardness, Corrosion Behavior, and Microstructural Characteristics of a Selective Laser Melted 17-4 PH Steel," Corrosion, vol. 78, no. 6, pp. 465–472, Jun. 2022, doi: 10.5006/3962.

[8] K. Wada, J. Yamabe, and H. Matsunaga, “Mechanism of hydrogen-induced hardening in pure nickel and in a copper–nickel alloy analyzed by micro Vickers hardness testing,” Materials Science and Engineering: A, vol. 805, p. 140580, Feb. 2021, doi: 10.1016/j.msea.2020.140580.

[9] C. F. Tan and M. R. Said, “Effect of Hardness Test on Precipitation Hardening Aluminium Alloy 6061-T6,” Chiang Mai J. Sci., p. 11.

[10] M. Z. Butt et al., “Nitrogen Ions Implantation in W-Based Quad Alloy: Structure, Electrical Resistivity, Surface Roughness and Vickers Hardness as a Function of Ion Dose,” Metals and Materials International, vol. 27, no. 9, pp. 3342–3358, Sep. 2021, doi: 10.1007/s12540-020-00861-z.

[11] S. C. Krishna, N. K. Gangwar, A. K. Jha, and B. Pant, “On the Prediction of Strength from Hardness for Copper Alloys,” Journal of Materials, vol. 2013, pp. 1–6, Apr. 2013, doi: 10.1155/2013/352578.

[12] M. Salandre, S. Garabedian, G. Gaillard, T. Williamson, and T. Joffre, “Development of a New Tooling Steel (L40) for Laser Powder Bed Fusion: Influence of Particle Size Distribution and Powder Atomization on Mechanical Performance,” Adv Eng Mater, vol. 23, no. 9, p. 2100350, Sep. 2021, doi: 10.1002/adem.202100350.

[13] "Grain boundary strengthening - Wikipedia", En.wikipedia.org, 2022. [Online]. Available: https://en.wikipedia.org/wiki/Grain_boundary_strengthening. [Accessed: 21- Jul- 2022].

[14] B. Zhang et al., “An efficient framework for printability assessment in Laser Powder Bed Fusion metal additive manufacturing,” Additive Manufacturing, vol. 46, p. 102018, Oct. 2021, doi: 10.1016/j.addma.2021.102018.

[15] J. Inoue, S. Nambu, Y. Ishimoto, and T. Koseki, “Fracture elongation of brittle/ductile multilayered steel composites with a strong interface,” Scripta Materialia, vol. 59, no. 10, pp. 1055–1058, Nov. 2008, doi: 10.1016/j.scriptamat.2008.07.020.

[16] "What is Bainite - Bainitic Steel - Definition | Material Properties", Material Properties, 2022. [Online]. Available: https://material-properties.org/what-is-bainite-bainitic-steel-definition/. [Accessed: 14- Jun- 2022].

[17] "Grain boundary strengthening - Wikipedia", En.wikipedia.org, 2022. [Online]. Available: https://en.wikipedia.org/wiki/Grain_boundary_strengthening. [Accessed: 14- Jun- 2022].

[18] “Properties and Selection: Irons, Steels, and High-Performance Alloys,” p. 2521.

[19] "Bainite | Metallurgy for Dummies", Metallurgyfordummies.com, 2022. [Online]. Available: https://www.metallurgyfordummies.com/bainite.html. [Accessed: 14- Jun- 2022].